INT. J. NUM. METH. HEAT FLUID FLOW, VOL. 3, 187–204 (1993)

A NUMERICAL STUDY OF DEVELOPING RADIAL FLOW WITH ROTATION

SHIN FANN AND WEN-JEI YANG

Department of Mechanical Engineering and Applied Mechanics, University of Michigan, Ann Arbor, Michigan 48109, USA

ABSTRACT

A numerical study is performed to investigate flow instability phenomena in a square channel with steady, laminar throughflow. The channel rotates around an axis perpendicular to the channel longitudinal axis. The flow field extends from the channel entrance to a distance of 120 to $600D_h$. The range of Reynolds number is $Re = 300$–2000. The inlet flow velocity is assumed uniform. Surface vorticity intensity is introduced to indicate the variation of vortices. It is revealed that at intermediate Reynolds numbers ($680 > Re > 300$), the flow is characterized by three vortex patterns: at slow rotation there is one vortex pair; at intermediate rotation a secondary vortex, in addition to the original vortex, emerges near the trailing wall and then breaks down downstream; and at rapid rotation the secondary vortex does not exist with the flow being restabilized to form a single-pair vortex pattern. At low Reynolds numbers ($Re \leqslant 300$), the flow exhibits a single-pair vortex pattern, while at high Reynolds numbers ($Re \geqslant 680$), the flow experiences the emergence and breakdown of a secondary vortex, but no restabilization is found with an increase in the rotational speed. It is also disclosed that the variation of the vortices is related to the distance from the inlet.

KEY WORDS Flow instability Laminar flow Radial rotation

NOMENCLATURE

a	channel height in the y-direction, m
b	channel width in the z-direction, m
D_h	hydraulic diameter, m
f	friction factor
H	distance from rotational axis to inlet, m
h	convective heat transfer coefficient, $W/m^2\,K$
h^*	non-dimensional distance from rotational axis to inlet, $= H/a$
L_x	characteristic length in the x-direction, m
P	pressure, Pa
P^*	reduced pressure, $= P - (\rho\Omega^2R^2)/2$
P_c	characteristic pressure, $= \mu(U_0/a)$
p	dimensionless reduced pressure
Re	Reynolds number based on the channel height, $= U_0a/\nu$
Ro	Rossby number based on the channel height, $= \Omega a/U_0$
Ta	Taylor number $= Re\,Ro$
U, V, W	velocity components in the x-, y-, z-directions, respectively, m/sec
U_0	inlet mean velocity, m/sec
V_c, W_c	characteristic transverse velocity components in y- and z-directions, respectively, $= U_0/\eta$
u, v, w	dimensionless velocity components in (x, y, z) directions, respectively

0961–5539/93/030187–18$2.00

Received April 1992
Revised November 1992

u^*	numerical axial flow velocity value, $=1$
u_0	dimensionless mean axial flow velocity
X	axial distance measured from flow inlet, m
Y	coordinate perpendicular to the rotational axis, m
Z	distance along rotational axis, m
Y_c, Z_c	characteristic lengths in y- and z-directions, $= a$ and b, respectively
x, y, z	dimensionless coordinate system with origin at centre of channel cross-section
x', y', z'	dimensionless coordinate system with origin at $z = -1/2$ and $y = 1/2$

Greek symbols

η	length ratio, $= L_x/a$
μ	dynamic viscosity, kg/m sec
ν	kinematic viscosity, m^2/sec
σ	surface vorticity intensity, see (13)
Ω	angular velocity of rotation, 1/sec
Ξ	axial velocity, 1/sec
ξ	non-dimensional axial vorticity
ξ_c	characteristic axial vorticity, $= U_0/\eta a$
ζ	aspect ratio, $= b/a$

Subscripts

c	characteristic quantity
o	at inlet
w	on wall
x	local value

INTRODUCTION

The influence of rotation on fluid flows, such as terrestrial flow[1] and flows in rotating machinery[2] has attracted considerable attention, especially the vortex induced by the Coriolis force and flow instability in rotating channels. Hart[3] was the first to conduct experiments on flow instability in a rotating channel flow. Flow visualization with the dye injection method was carried out in a rectangular channel with an aspect ratio (b/a) of about 7 at slow to relatively rapid rotational speeds. Experimental results demonstrated the existence of three regimes in rotating channel flow. A double-vortex secondary flow prevails at slow rotational speeds; an instability in the form of longitudinal roll cells occurs at intermediate rotational speeds; and a restabilization of flow to a Taylor–Proudman regime happens at high rotational speeds. The Taylor–Proudman regime refers to a flow region in which axial velocity profiles do not vary along rotational axis, and is similar to that in the Ekman layer[1]. Hart also performed a linear stability analysis, using the Galerkin method to determine the onset of roll cells in a rotating, plane Poiseuille flow which corresponds to the limiting case of rectangular channel with an infinite aspect ratio. Results were in general agreement with experimental data.

Johnston *et al.*[4] conducted experiments on a fully-developed turbulent flow in a channel ($\zeta = 7.14$) rotating radially at a steady speed and found three stability-related phenomena: (i) a reduction (or an increase) in the rate of wall-layer streak bursting in locally stabilized (or destabilized) wall layers; (ii) total suppression of transition to turbulence in a stabilized layer; (iii) development of large-scale roll cells on the destabilized side of the channel induced by the growth of Taylor–Gortler vortex instability. They suggested that the Richardson number might be an appropriate local stability parameter, and that local effects of rotational stabilization, such as a reduction of turbulence stress in wall layers, can be related to the Richardson number in a simple way.

Lezius and Johnston[5] performed a theoretical analysis of laminar roll-cell instability in a rotating channel flow. The investigation included a linear stability analysis for the onset of laminar roll cells in a rotating, plane Poiseuille flow by means of the finite difference method. The specific results obtained indicated that the critical disturbance occurs at $Re = 88.53$ and $Ro = 0.5$. However, at higher Reynolds numbers, the unstable conditions can be found in the

range of $0 < Ro < 3$. In general, these results predicted flow instability at a lower Reynolds number for a given Rossby number than the results of Hart[3]. A linear stability analysis was carried out for the onset of roll-cell instability in a turbulent, plane Poiseuille flow subjected to a radial rotation. Although the analysis was linear using a turbulence model, the results were in good agreement with experiments[4]. Speziale and Thangam[7] extended Speziale[6] to a numerical study on the secondary flow and roll-cell instability in a rotating channel with an aspect ratio of eight, $0 < Re < 500$ and $0.0001 < Ro < 3$. The roll-cell and Taylor–Proudman regimes which led to a substantial distortion of axial velocity profiles were found. Results were in agreement with the existing experimental data and theoretical predictions. The critical point at $Re = 110$ and $Ro = 0.5$ is higher than the prediction of Lezius and Johnston[5].

Hwang and Jen[8] reported a numerical investigation of heat transfer in hydrodynamically and thermally fully-developed, laminar flow in rotating isothermal ducts. The temperature distribution equation for a fully-developed flow in a stationary passage was modified to evaluate the temperature field in a rotating duct. It was disclosed that flow instability (the emergence of a secondary vortex) occurred at $25{,}500 \leqslant Re\,Ta < 20{,}000$ for an aspect ratio of $\zeta = 1.0$ and at $Re\,Ta \geqslant 82{,}000$ for $\zeta = 2.0$. It was found that a secondary vortex may appear in a certain range of $Re\,Ta$ but may disappear at the same value of $Re\,Ta$. Jen *et al.*[9] numerically investigated a simultaneously developing laminar flow in a radially rotating isothermal square channel to a length of $0.2–0.25(D_h Re)$ and found a secondary vortex breakdown to occur at various Reynolds numbers.

Fann and Yang[10] and Fann *et al.*[11] numerically studied transport phenomena in the entrance region of radially rotating heated channels with different aspect ratios. The thermal boundary conditions included the uniform wall temperature and uniform wall heat flux. The computation length was from the channel entrance to about 20 times channel height. Secondary vortices were found to appear immediately after the entrance with their number varying with the geometry, Reynolds number and location along the channel.

The present study concerns with flow instability phenomena in a square channel in radial rotation with uniform inlet velocity. The computation is carried out up to a distance of 120 to 600 D_h in order to cover the entire process of vortex evolution. The variation of vortex patterns is indicated by surface vorticity intensity. The velocity–vorticity method is employed in the formulation[12,13]. The resulting parabolic equations are solved to determine the axial velocity and axial vorticity explicitly[14].

THEORETICAL ANALYSIS

The physical system to be studied is shown in *Figure 1a*. It consists of a flow through a square channel rotating at a constant speed Ω about an axis normal to the longitudinal direction of the channel. The velocity components in the x-, y- and z-directions are u, v, and w, respectively. In order to normalize the governing equations, the velocity, pressure, coordinate variables, and geometrical dimension are non-dimensionalized by dividing their respective characteristic quantities as follows:

$$x = \frac{X}{L_x}, \quad y = \frac{Y}{a}, \quad z = \frac{Z}{b}, \quad u = \frac{U}{U_0}, \quad v = \frac{V}{V_c}, \quad w = \frac{W}{W_c},$$

$$p = \frac{P^*}{P_c}, \quad \eta = \frac{L_x}{a}, \quad \zeta = \frac{b}{a}, \quad \xi = \frac{\Xi}{\xi_c}$$

Here, P^* is the reduced pressure. The characteristic quantities, denoted by the subscript c, are defined in the nomenclature. The axial vorticity transport equation is introduced to eliminate the pressure gradient terms in both the y- and z-direction momentum equations. The

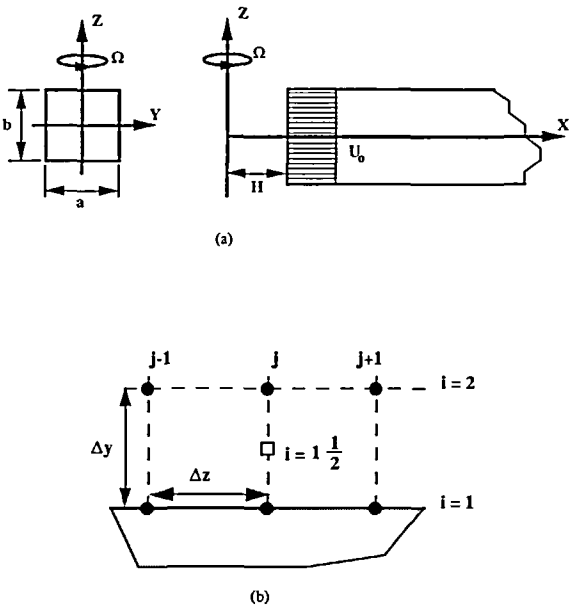

Figure 1 (a) Coordinate system on a rotating channel and (b) nodes for boundary vorticity

non-dimensional axial vorticity can be expressed as:

$$\xi = \frac{\partial w}{\partial y} - \frac{1}{\zeta}\frac{\partial v}{\partial z} \tag{1}$$

The continuity equation and (1) may be combined to yield the velocity equations for v and w. Under the assumptions of constant physical properties, the governing equations for an incompressible, steady, laminar flow read (details in Fann and Yang[10]):

(*a*) x-*momentum equation:*

$$u\frac{\partial u}{\partial x} + v\frac{\partial u}{\partial y} + \left(\frac{1}{\zeta}\right)w\frac{\partial u}{\partial z} = \frac{-1}{Re}\frac{\partial p}{\partial x} + 2(Ro)v + \left(\frac{\eta}{Re}\right)\frac{\partial^2 u}{\partial y^2} + \left(\frac{\eta}{\zeta^2 Re}\right)\frac{\partial^2 u}{\partial z^2} \tag{2}$$

(*b*) *Axial velocity transport equation:*

$$u\frac{\partial \xi}{\partial x} + v\frac{\partial \xi}{\partial y} + \left(\frac{1}{\zeta}\right)w\frac{\partial \xi}{\partial z} + \frac{\partial u}{\partial y}\frac{\partial w}{\partial x} - \left(\frac{1}{\zeta}\right)\frac{\partial u}{\partial z}\frac{\partial v}{\partial x} - \xi\frac{\partial u}{\partial x}$$
$$= 2\left(\frac{\eta^2 Ro}{\zeta}\right)\frac{\partial u}{\partial z} + \left(\frac{\eta}{Re}\right)\frac{\partial^2 \xi}{\partial y^2} + \left(\frac{\eta}{\zeta^2 Re}\right)\frac{\partial^2 \xi}{\partial z^2} \tag{3}$$

(*c*) *Poisson equations for the transverse velocities:*

$$\frac{\partial^2 v}{\partial y^2} + \frac{1}{\zeta^2}\frac{\partial^2 v}{\partial z^2} = -\frac{1}{\zeta}\frac{\partial \xi}{\partial z} - \frac{\partial^2 u}{\partial x\,\partial y} \tag{4}$$

$$\frac{\partial^2 w}{\partial y^2} + \frac{1}{\zeta^2}\frac{\partial^2 w}{\partial z^2} = \frac{\partial \xi}{\partial y} - \frac{1}{\zeta}\frac{\partial^2 u}{\partial x\,\partial z} \tag{5}$$

Because of a relatively strong inertia force in the axial direction, the second derivative (diffusion) terms in the x-direction may be neglected and these equations take a parabolic-elliptic form. This formulation is so-called the velocity–vorticity method[12]. The appropriate inlet and boundary conditions are:

$$\textit{at inlet:} \qquad u = 1.0, v = w = 0, \xi = 0 \tag{6}$$

$$\textit{at walls:} \qquad u = v = w = 0 \tag{7}$$

The pressure term can be decoupled as:

$$p(x, y, z) = \bar{p}(x) + p'(x, y, z)$$

By making the parabolic assumption[14], $\partial p'/\partial x \ll \mathrm{d}\bar{p}/\mathrm{d}x$, the axial pressure gradient is then given by:

$$-\frac{\partial p}{\partial x} = -\frac{\mathrm{d}\bar{p}}{\mathrm{d}x} = -f(x)$$

where $f(x)$ is determined by the constant flow rate constraint. A staggered mesh network is employed in the numerical analysis. The numerical method modified from Patankar[14] is used to determine the axial velocity and vorticity, and the Power-law scheme is employed (see Fann and Yang[10] for details). The axial velocity thus obtained must satisfy the continuity equation. Otherwise, a new axial pressure gradient is assumed and the computation is repeated for a new axial velocity, until the continuity equation is satisfied. The flow rate through each channel cross section is calculated using Simpson's rule.

$$\left| \frac{\int u^* \, \mathrm{d}y \, \mathrm{d}z - \int u_0 \, \mathrm{d}y \, \mathrm{d}z}{\int u_0 \, \mathrm{d}y \, \mathrm{d}z} \right| \leqslant 10^{-7} \tag{8}$$

where u^* is the numerical axial velocity value, and u_0 is the dimensionless mean axial flow velocity.

In (4) and (5), the second-order, centred difference method is employed to discretize the y and z derivatives, while the three-point backward difference method is used for the x derivatives. The criterion of convergence for transverse velocities is set as:

$$\max \left| \frac{v^n - v^{n-1}}{v^n} \right| \leqslant 5 \times 10^{-5} \tag{9}$$

where n is the iteration sequence number.

The numerical scheme used in treating the boundary vorticity is adopted from Chou[13] to improve the accuracy of computation up to the second order, as shown in *Figure 1b*.

$$\xi_{1,j} = -\xi_{2,j} + \frac{2w_{2,j}}{\Delta y} - \frac{v_{2,j+1} - v_{2,j-1}}{2\zeta \, \Delta z} + \mathrm{O}(\Delta y^2, \Delta z^2) \tag{10}$$

The line iteration method with an under-relaxation factor is utilized in the computations of u in order to improve the convergence speed. The point iteration method is employed in calculating ξ, v and w, while the three-point forward (or backward) finite difference scheme is used in the calculations of the axial velocity gradients for the friction factor.

The ranges of parameters used in the simulation are: (1) $Re = 300$–2000, and (2) $Ro = 0.001$–0.50. Because the region of vortex evolution in a rotating channel changes with the Reynolds number, the computation length is varied; e.g., 120 D_h for $Re \leqslant 350$, 200 D_h for $Re \leqslant 670$ and 600 D_h for $Re \geqslant 1000$. The eccentricity distance is 10 D_h. The mesh size used in computations is listed in *Table 1*, where the M and N represent the number of grid points in the y and z

Table 1 Mesh sizes used in numerical computations

	Re			
	300–400	500	600–700	1000–2000
$0.0 \leqslant Ro \leqslant 0.05$		41 × 41		41 × 41
$0.05 < Ro < 0.20$	45 × 45	45 × 45	45 × 45	45 × 45
$Ro \geqslant 0.20$	51 × 51	51 × 51	51 × 51	51 × 51
Ro	$Ro = 0.0$		$0.0 < Ro < 0.20$	$Ro \geqslant 0.20$
$\Delta X/a$	1/15		1/25	1/30

directions, respectively, and the $\Delta X/a$ is the grid space in the axial direction. The uniqueness and the mesh dependence of the numerical solutions are available in References 10, 11, 15. The sequence of computation is presented in Reference 11.

The friction factor f is defined as:

$$f = \frac{\mu\left(\overline{\frac{\partial U}{\partial N}}\right)_{\text{wall}}}{\frac{1}{2}\rho U_0^2} \tag{11}$$

f and Re can be combined to give:

$$f\,Re = 2\left(\overline{\frac{\partial u}{\partial n}}\right)_{\text{wall}} \tag{12}$$

where n denotes the dimensionless coordinate normal to the wall.

References 10 and 11 have disclosed the emergence of a secondary vortex initially emerges in the vicinity of the trailing wall. Hence, the evolution of the vortex can be monitored through a change in the boundary vorticity on the trailing wall whose intensity is defined as:

$$\sigma = \int_0^{1/2} \xi_{\text{Trailing wall}}\, dz \tag{13}$$

The surface vorticity intensity is integrated from $z' = 0$ to 1/2 to distinguish the condition of no secondary vortex from that of a symmetric secondary vortex. In spite of the asymmetry of secondary vortices under certain circumstances, the variation of vortex can still be illustrated by this form of integration. The surface vorticity intensity replaces the friction factor as an indication for the presence of a secondary vortex for the following reasons: (1) the friction factor is not sensitive to an inception and evolution of a small secondary vortex, (2) the surface vorticity intensity can recognize the pattern of a secondary vortex when it becomes asymmetric, and (3) the surface vorticity intensity is much less sensitive to the grid number than the friction factor so that coarser meshes may be used in computations.

RESULTS AND DISCUSSION

Numerical computations are carried out to determine the flow patterns, surface vorticity intensity and friction factor. *Figure 2* shows the critical points for an inception of flow instability on a plot of the critical Rossby number against the Reynolds number. *Table 2* lists the range of critical Rossby numbers *versus* the Reynolds number. The first critical point is defined as the condition

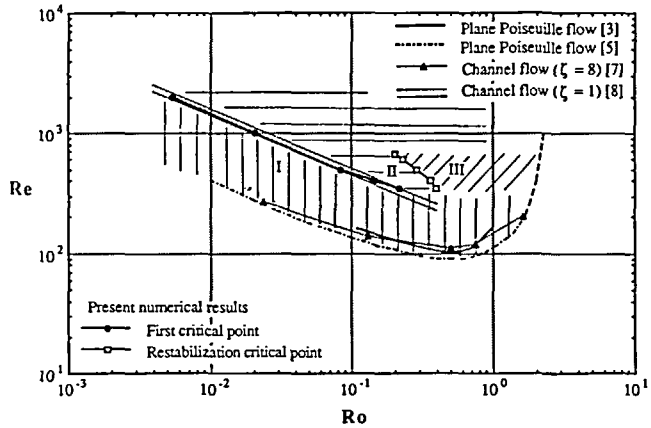

Figure 2 The critical points for flow instability

Table 2 Range of critical Rossby numbers

	Re				
	350	400	500	1000	2000
Frist critical point	0.2125–0.2150	0.1400–0.1425	0.0825–0.0850	0.0205–0.0210	0.00525–0.00550
	350	400	500	600	670
Restabilization critical point	0.3925–0.3950	0.3575–0.3600	0.2850–0.2875	0.2300–0.2325	0.2000–0.2025

for an inception of a secondary vortex, while the restabilization critical point corresponds to the condition for the disappearance of the secondary vortex. The $Re\,Ta$ value for the first critical point in the present study ranges from 21,000 to 26,000, which is in agreement with the predictions of Hwang and Jen[8], while the $Re\,Ta$ value for the restabilization critical point lies in the range 48,000 to 90,400. The determination of these critical points is described later, but the lowest critical Reynolds number and its corresponding Rossby number are not determined due to the complexity in computations. It is seen in *Figure 2* that the loci of the first and restabilization critical points define Regimes I, II and III. Regime I is the domain in which only one pair of vortices exist throughout the entire channel. In Regime II, secondary vortices appear but break down as it moves downstream. Regime III corresponds to the restabilization zone where a pair of small vortices emerge near the trailing wall but are soon destroyed, never growing to form a secondary vortex.

This observation implies the existence of three different flow pattern evolutions for the Reynolds number in the range of 300 to 200: (i) a pair of principal vortices appear at slow rotation; i.e. Regime I; (ii) an increase in the rotational speed induces the generation of secondary vortices around the centreline ($z' = 0.5$) near the trailing wall which eventually break down; (iii) as the rotational speed is further increased, a generation of secondary vortices is inhibited with the flow being restabilized to exhibit a pair of principal vortices; i.e. Regime III. The breakdown of secondary vortices was also reported in Reference 9.

Regime I (principal vortex) prevails for flows at the Reynolds numbers lower than 300. Two distinct vortex patterns exist when the Reynolds numbers exceeds 680: (i) Regime I principal vortex pattern at low rotational speeds, and (ii) Regime II with the generation followed by

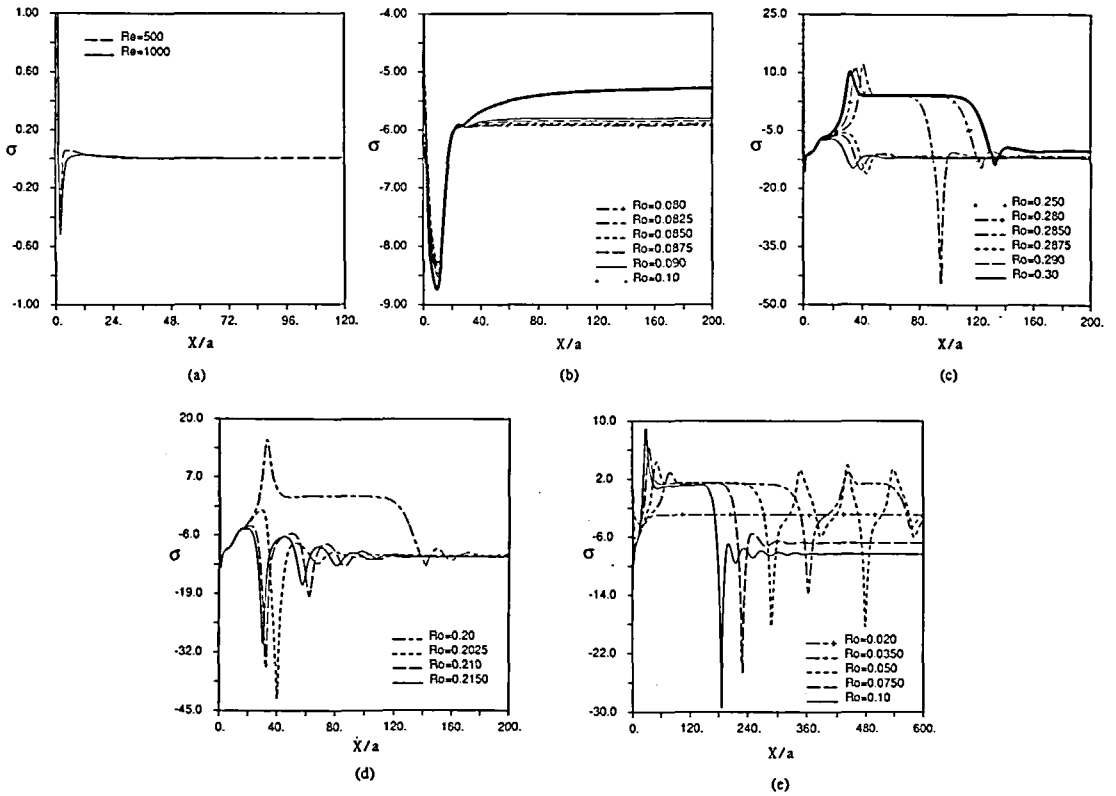

Figure 3 Surface vorticity intensity distributions along the channel for flow at (a) $Re = 500$, 1000 and $Ro = 0.00$, (b) $Re = 500$ and $Ro = 0.080$–0.10, (c) $Re = 500$ and $Ro = 0.25$–0.3, (d) $Re = 670$ and $Ro = 0.20$–0.2150, and (e) $Re = 1000$ and $Ro = 0.020$–0.10

collapse of secondary vortices at higher rotational speeds. Unstable flow occurs only in range of $680 > Re > 300$. Similar findings are reported in References 3–7 for the rotating ducts of high aspect ratios as well as the square channel only one pair of secondary vortices. These references report no finding of vortex breakdown. In the interest of brevity, representative cases of $Re = 500$, 670 and 1000 are presented here for discussing flow instability phenomena:

Stationary case

Viscosity and non-slip boundary conditions cause the flow to be retarded near the walls and the fluid mass to be brought into the channel core in order to satisfy the continuity. In the absence of gravity and rotation, the transverse flow velocity is directed towards the channel centre, resulting in positive values for both the boundary vorticity and the surface vorticity intensity at the trailing wall from $z' = 0.0$ to $z' = 0.5$. After the flow enters the channel, the transverse flow velocity near the walls changes drastically. The change diminishes rapidly as soon as the flow begins to retard. That is why the surface vorticity intensity approaches an asymptotic value of slightly above zero in a short distance from the inlet, as seen in *Figure 3a*. *Figure 4a* depicts that the friction factor reaches an asymptotic value at further downstream than the surface vorticity intensity.

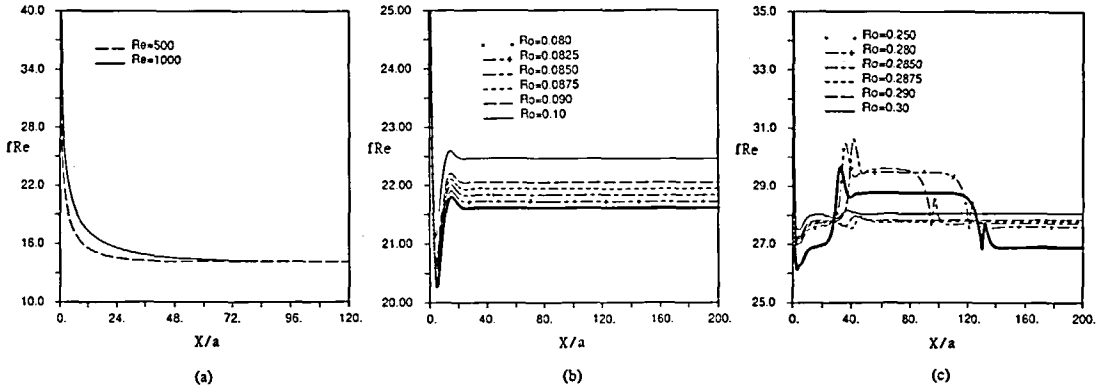

Figure 4 Circumferentially-averaged friction factor distributions along the channel for flows at (a) $Re = 500$, 1000 and $Ro = 0.0$, (b) $Re = 500$ and $Ro = 0.080$–0.10, and (c) $Re = 500$ and $Ro = 0.25$–0.3

Principal vortex case (Regime I)

The vortex pattern appears as soon as the flow enters a rotating channel[10,11]. Even a very slow rotation can induce the principal vortices which cause a sharp drop in the surface vorticity intensity to a negative value, as shown in *Figure 3b*. It results from an interaction of viscous and rotational effects with viscosity retarding the flow and rotation inducing the longitudinal vortices in the channel cross-section. Since a large amount of mass near the walls must move to the channel core while the transverse flow cannot drastically deform like in the stationary case, mass is carried by the vortices towards the central core. Therefore, the transverse velocity near the trailing wall, especially the w component, is high near the entrance resulting in a negative boundary vorticity (due to a negative w in the region of $y' < 0.5$ and $0 \leqslant z' \leqslant 0.5$) and a negative surface vorticity intensity. As the flow proceeds downstream, less mass needs to be moved, and the transverse velocity diminishes. This results in a rebound in the distribution of σ. If rotation is too slow to induce secondary vortices, the flow velocity profiles become invariant. Eventually, mass balance is achieved with the surface vorticity intensity approaching a constant value; e.g., $Ro = 0.080$ in *Figure 3b*. *Figures 5a* and *5b* depict a pair of the principal vortices which prevail over a long distance.

The first critical point of flow at $Re = 500$ can be determined from *Figure 3b*. Before the Rossby number reaches 0.080, the asymptotic value of the surface vorticity intensity is diminished with an increase in the rotational speed (not shown). Once Ro exceeds 0.080, the asymptotic value of σ increases as the rotational speed is increased. The increase of σ is caused by the appearance of secondary vortice. The Rossby number where the σ asymptotic value begins to grow is defined as the first critical point. In the case of $Re = 500$, the first critical point is between $Ro = 0.0825$ and 0.0850.

Secondary vortex case (Regime II)

When the rotational speed exceeds the critical value, a pair of small vortices begin to emerge around the centerline near the trailing wall. It is depicted in *Figure 3b* that all curves undergo a steep fall followed by a very steep rise, irrespective of Ro values. At $Re = 500$, no secondary vortex is seen at $Ro = 0.080$, while it becomes obvious in pair at $Ro = 0.10$. After the rebound, σ continues to grow in the $Ro = 0.10$ case because the secondary vortex rotates in the direction opposite to that of the principal vortices. Hence, the surface vorticity intensity will grow once the secondary vortex appears. If the secondary vortex is strong enough, σ will approach a

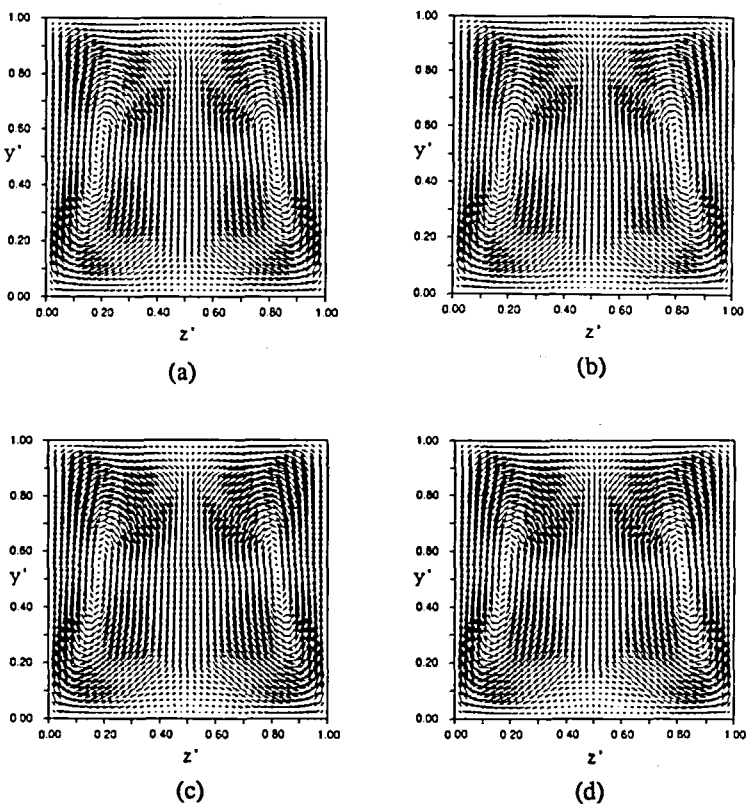

Figure 5 Cross-sectional transverse flow velocity distribution for $Re = 500$, $Ro = 0.080$ at (a) $X = 40a$ and (b) $X = 120a$, and $Ro = 0.10$ at (c) $X = 40a$ and (d) $X = 120a$

positive constant, otherwise it would remain negative. *Figures 5c* and *5d* depict flows with small secondary vortices at $Re = 500$ and $Ro = 0.10$. When the rotational speed is further increased, the secondary vortices grow stronger and faster, and σ overshoots into the positive region after a rebound, see $Ro = 0.250$, 0.280 and 0.285 in *Figure 3c*. The σ growth peaks out followed by a rapid fall and then levels off. Similar to the principal vortex case, it is caused by the redistribution of mass induced by the secondary vortex in order to satisfy mass continuity requirement. *Figure 3c* also discloses that the peak of σ overshoots moves downstream with an increase in the Rossby number (rotational speed). The asymptotic values of σ following overshoots are almost the same irrespective of the Rossby number. As it proceeds downstream, vortex flow undergoes another change, namely a breakdown of secondary vortices. It results in a decline, oscillation and levelling off of surface vorticity intensity, as seen in *Figure 3c* at $Ro = 0.250$, 0.280 and 0.285. The location where σ begins to fall moves upstream with an increase in the Rossby number. This phenomenon was also discussed in Reference 9 and will be discussed later.

The effect of secondary vortices also appears in the friction factor distribution, as shown in *Figures 4b* and *4c*. *Figure 4b* display that all fRe curves are similar in shape irrespective of secondary vortices in presence or not. However, only in flows with strong secondary vortices, their fRe curves in *Figure 4c* resembles the σ curves in *Figure 3c*. *Figures 6a–6h* reveal that mass redistribution induced by secondary vortices strongly affects the flow in the trailing half ($y' < 0.5$), especially in the area near the centreline.

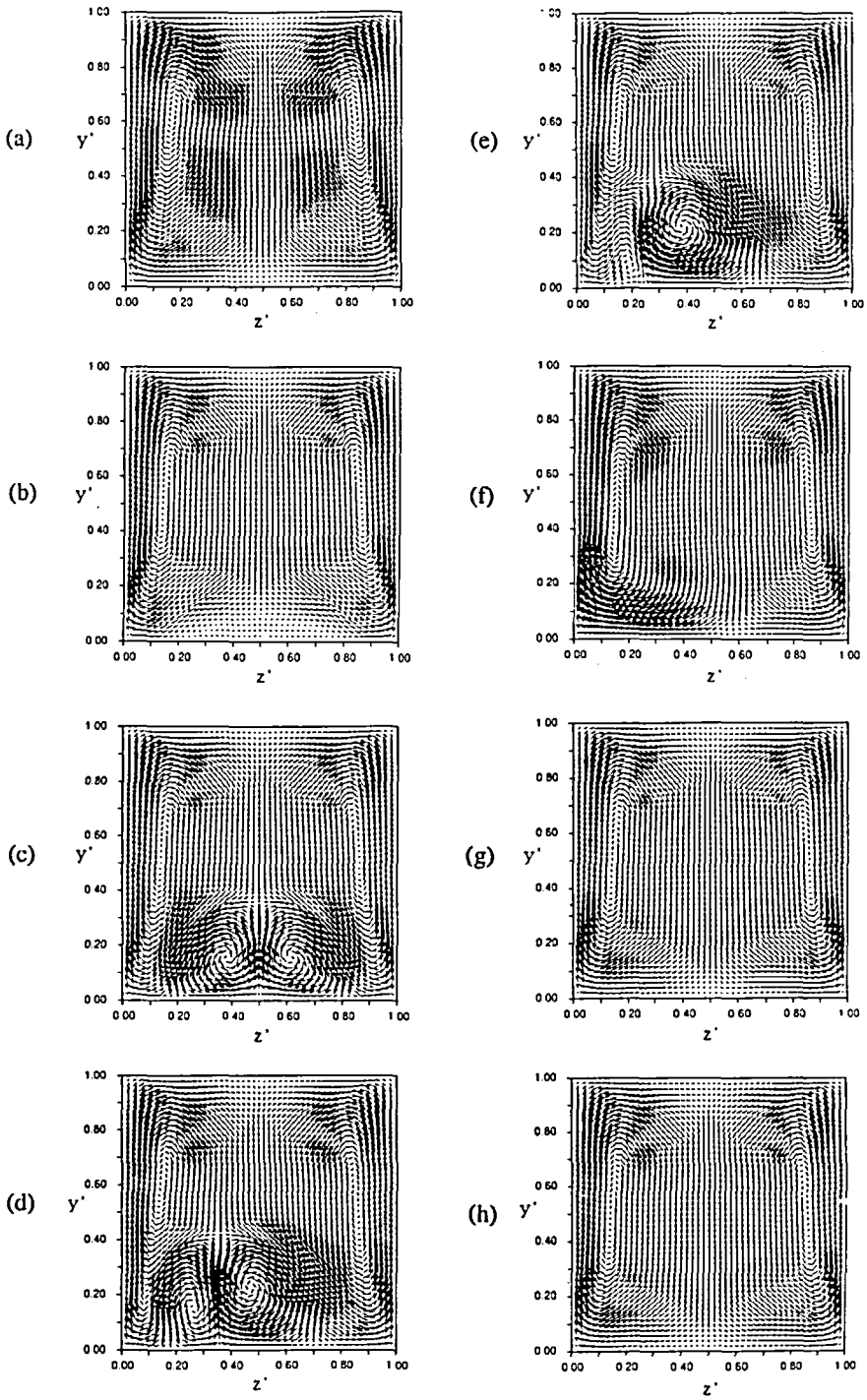

Figure 6 Cross-sectional transverse flow velocity distribution for flows at $Re = 500$, $Ro = 0.285$, (a) $X = 4a$, (b) $X = 24a$, (c) $X = 40a$, (d) $X = 88a$, (e) $X = 92a$, (f) $X = 96a$, (g) $X = 120a$ and (h) $X = 200a$

Restabilization case (Regime III)

When the rotational speed is further increased, another critical state is reached in which the secondary vortex fails to form with the surface vorticity intensity behaving quite differently from that discussed above. It is seen in *Figure 3c* at $Ro = 0.2875$, 0.290 and 0.30 that after a flow enters the channel, its transverse velocity near the trailing wall is large but diminishes to form a rebound of σ as the flow proceeds downstream. However, at certain distance downstream, the principal vortex grows stronger and engulfs smaller secondary vortices, while the surface vorticity intensity diminishes. Eventually, mass balance is achieved, vortex flow becomes invariant, and surface vorticity intensity reaches a constant. It should be noted that the higher the Rossby number, the sooner the surface vorticity intensity becomes stable. This means that a strong principal vortex contributes to a quicker mass balance. The observation is supported by *Figure 4c* demonstrating that a strong principal vortex contributes to a smaller overshoot in the friction factor distribution for restabilization. *Figures 7a* through *7e* depict a series of variation in vortices along the channel at $Ro = 0.2875$ and $Re = 500$. In comparison with *Figures 6a–6h* at $Ro = 0.285$ and $Re = 500$, both flows share the same patterns until $X = 24a$ beyond which the smaller vortices adjacent to the trailing wall disappear in the case of $Ro = 0.2875$. However, no restabilization phenomenon is found in flows with a higher Reynolds number ($Re \geqslant 680$). It is conjectured that under such a high-speed flow the inertia of the secondary vortex becomes strong enough not to be integrated into the principal vortex. From the behaviour of flows at $Ro = 0.2850$ and 0.2875, the restabilization critical point is determined.

Another interesting phenomenon is disclosed in flow at $Re = 670$ which is close to the upper limit of the Regime II. As depicted in *Figure 3d*, the σ curves for flows at $Ro \geqslant 0.2025$ exhibit an oscillation which is damped out downstream. The sharp drop of σ in *Figure 3d* is not caused by the breakdown of secondary vortices like that in *Figure 3e*. It results from the separation and disappearance of smaller vortices as seen in *Figure 7b*. The variation of this small vortex pair is illustrated in *Figures 8a* through *8f*, where they drift apart and eventually integrated into the principal vortex. The weak oscillation of σ after $X = 48a$ in *Figure 3d* is induced by the oscillation of the principal vortex pair.

Breakdown of secondary vortices

Figure 3e shows two kinds of breakdown of secondary vortices, depending upon the Rossby number. In the Regime II of *Figure 2*, the breakdown process at a lower rotational speed, experiences a series of asymmetric deformation: an evolution in which stronger secondary vortices engulfing the weaker ones, destruction and reproduction of secondary vortices, as seen in *Figure 3e* at $Ro = 0.035$ and 0.05. The same kind of vortex breakdown is also found in the case of $Re = 500$ and $Ro = 0.20$ (not shown). A typical process is illustrated in *Figure 9* for $Re = 1000$ and $Ro = 0.05$. It reveals that (a) the secondary vortex pair are practically symmetrical at $X = 200a$, (b) the one in the right half region grows stronger into the left half region at $X = 260a$, (c) at $X = 300a$, the secondary vortex pair disappear, (d) the pair emerge again at $X = 360a$, (e) the vortex in the left half region grows stronger into the right half region, just opposite to that observed at $X = 260a$, and (f) through (j) with the same phenomena observed in (a) through (e) repeating in $X = 400a$–$600a$. This periodical vortex change persists downstream.

It is also discussed that the period of vortex change is shortened with an increase in the Rossby number; for example from $Ro = 0.035$ to 0.05 in *Figure 3e*. However, as the rotational speed is further increased from $Ro = 0.075$ to 0.10 in *Figure 3e* or $Ro = 0.250$, 0.280 and 0.285 in *Figure 3c*, the magnitude of re-production secondary vortices diminishes. Eventually, secondary vortices re-production is terminated while the principal vortex pair oscillate and gradually stabilize. This is the second kind of vortex breakdown which takes place much faster than the first kind. *Figure 6c* through *6g* demonstrate a typical example of the second kind of vortex breakdown with only one evolution. Since the vortex flow pattern undergoes numerous

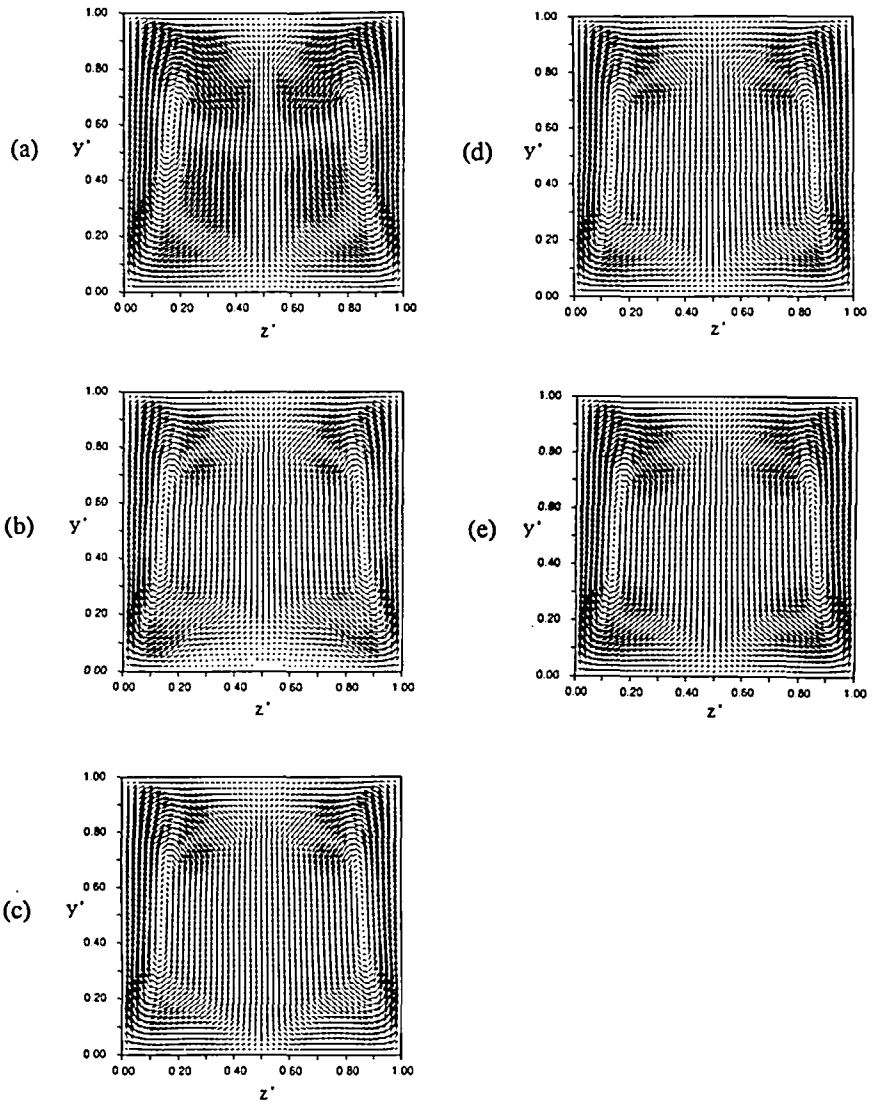

Figure 7 Cross-sectional transverse flow velocity distribution for flows at $Re = 500$, $Ro = 0.2875$, (a) $X = 4a$, (b) $X = 24a$, (c) $X = 40a$, (d) $X = 120a$ and (e) $X = 200a$

variations, it is inappropriate to treat the rectangular or square channel flow with rotation to have a symmetric flow pattern with respect to the channel centreline over the entire flow passage, or to study only one-half of the flow cross-section in a fully-developed flow region. In general, the symmetry of secondary vortices prevails only up to a distance 0.2 (a *Re*) from the entrance.

Mechanism of vortices

Until now, the mechanism of variation of the Coriolis-induced vortices is not fully understood. Some insight into such a mechanism is presented in the following: the axial flow velocity profile in the absence of rotation takes a symmetrical form with respect to the channel centreline as

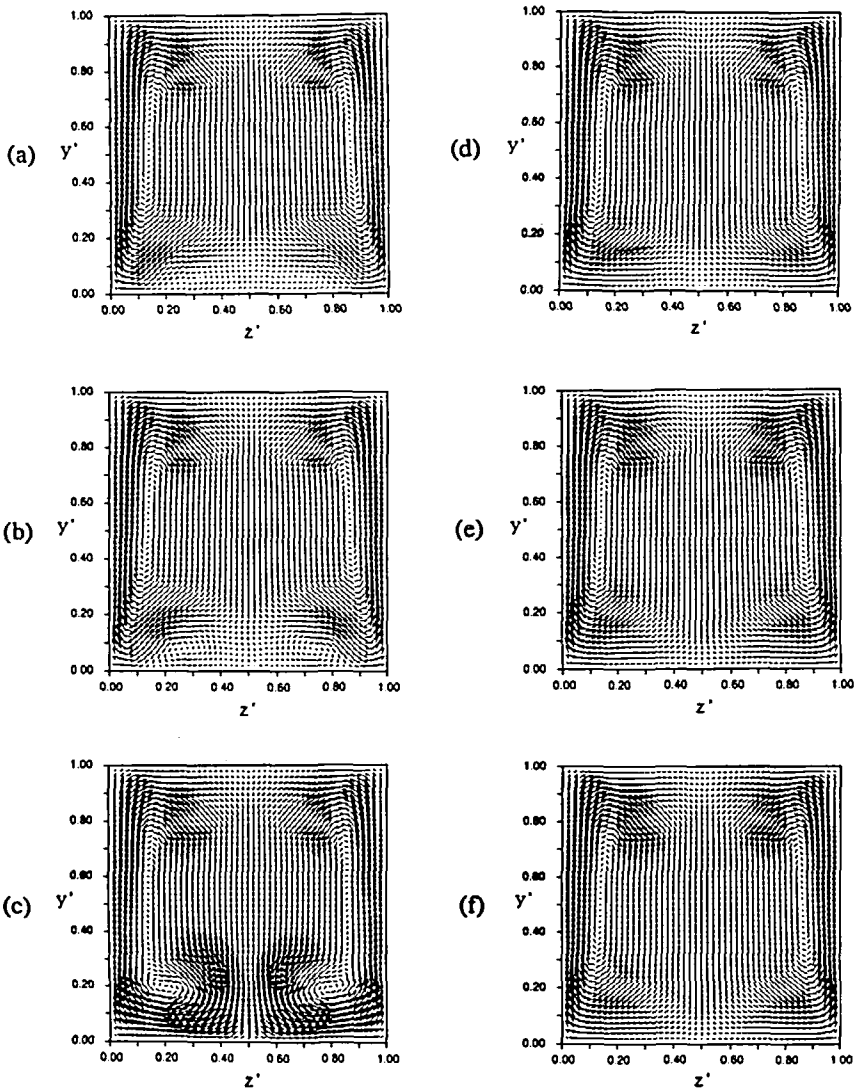

Figure 8 Cross-sectional transverse flow velocity distribution for flows at $Re = 670$, $Ro = 0.2025$, (a) $X = 20a$, (b) $X = 28a$, (c) $X = 40a$, (d) $X = 48a$, (e) $X = 60a$, and (f) $X = 120a$

shown in *Figure 10a*. The initiation of radial rotation induces the velocity profile to deform forming an asymmetrical tip pointing towards the trailing wall as depicted in *Figure 10b*. It is induced by the principal vortex that transports fluid particles in the central core of the channel towards the trailing wall, as the flow proceeds downstream. The change in the velocity profile is accompanied by an alteration in its slope and consequently a variation in the shear stress, especially in the region adjacent to the trailing wall. *Figure 10c* shows all forces acting on a fluid particle whose velocity is identified by a dot on the velocity profile in *Figure 10b*. They include the Coriolis force F_c, inertia force F_I and shear force τ that determine the motion of the particle. Here, the inertia force refers to the driving potentials such as pressure gradient and centrifugal force. In the present study, the transverse motion of fluid particles in the cross-section is induced

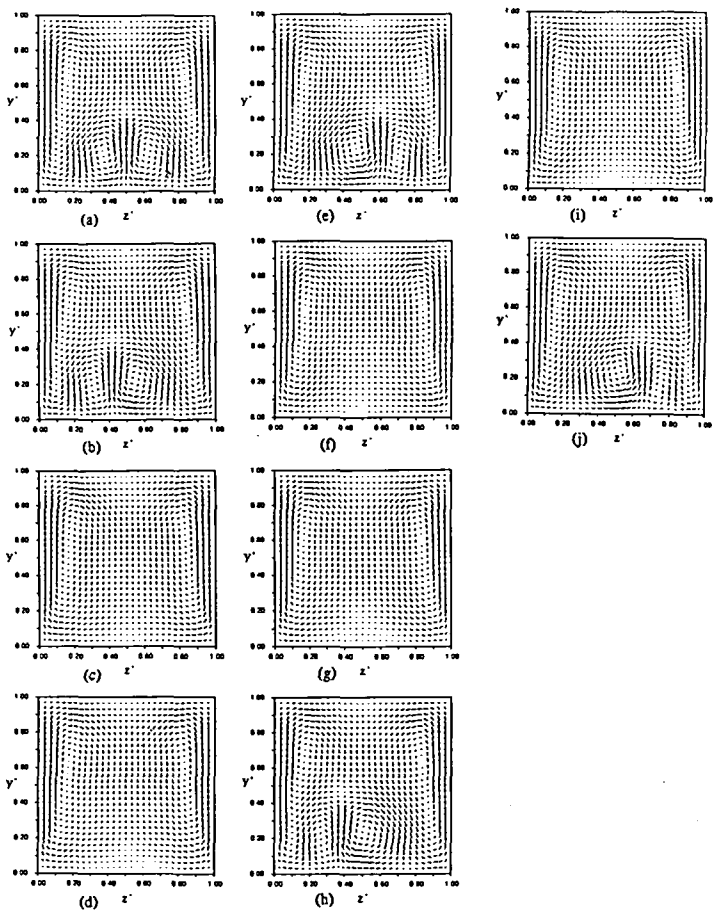

Figure 9 Cross-sectional transverse flow velocity distribution for flows at $Re = 1000$, $Ro = 0.05$, (a) $X = 200a$, (b) $X = 260a$, (c) $X = 300a$, (d) $X = 320a$, (e) $X = 360a$, (f) $X = 400a$, (g) $X = 420a$, (h) $X = 460a$, (i) $X = 500a$ and (j) $X = 560a$

by the Coriolis force, resulting from the interaction of rotation and axial flow velocity. Due to a strong non-linear interaction among these forces, it is difficult to identify which force induces or demolishes the secondary vortex. In the principal vortex case, the Coriolis force in the negative y-direction, F_{cy}, is probably the driving force to bring about the principal vortex which transports the fluid particles against rotation in the region near the channel centreline and trailing wall. Notice that F_{cy} always acts in the negative y-direction, because of positive axial velocity. At a lower rotational speed, the fluid particles at the channel centreline ($z' = 1/2$) move slowly towards the trailing wall. The motion of fluid particles is retarded in the intersection region of the trailing wall with the centreline.

As the rotational speed is increased, the vortex strength grows with these retarded particles being dragged to move by the shear force. In the course of flow along the channel, if the vortex strength reduces to such an extent the shear force cannot drag those retarded particles, a small vortex of opposite rotation is initiated in order to satisfy mass continuity, see *Figure 10e*. Should this small vortex survive the interaction of the oppositely-rotating principal vortex, it becomes the secondary vortex. The mechanism of reversal in the direction of particle motion is probably

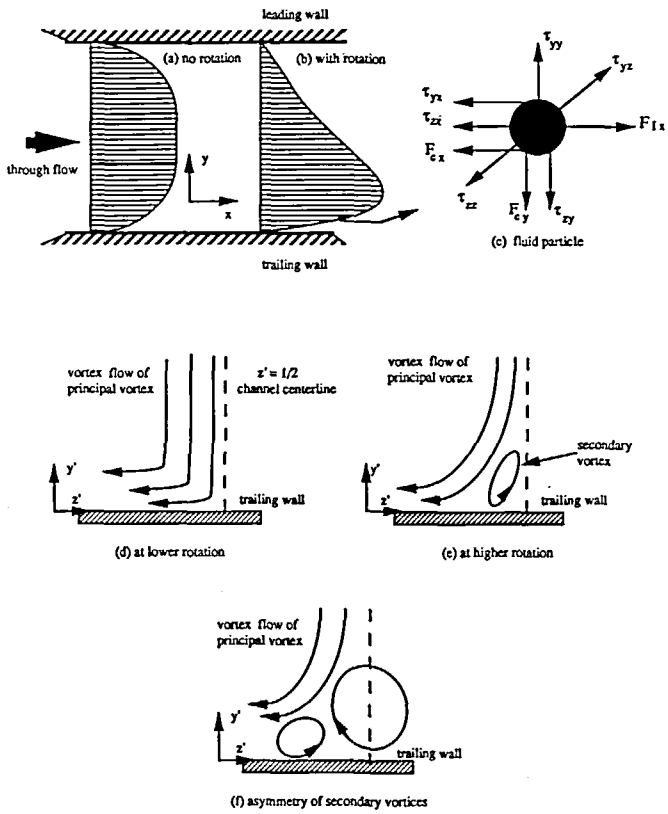

Figure 10 Motion of fluid particles near the trailing wall and channel centreline

due to increases in the magnitude of τ_{zy} and τ_{yy} in the positive y-direction and that of τ_{yz} and τ_{zz} in the positive z-direction. However, if the flow is in the range of an intermediate Reynolds number (that is, $300 < Re < 680$), the Coriolis force becomes dominant again with an increase in the rotational speed. Under such circumstances, the strength of the principal vortex would be strong enough to carry the retarded particles, thus destroying the small vortex. This is the phenomenon of flow restabilization. *Figures 6* and *7* display the difference between the development and destruction (i.e., restabilization) of the secondary vortex. In *Figures 6a* through *6h*, a smaller vortex appearing at $X = 24a$ continues to grow in the course of flow down the channel, thus forming the secondary vortex. In contrast, the smaller vortex observed at $X = 24a$ disappears in *Figures 7a* through *7e*; i.e., flow restabilization.

If the Reynolds number is increased beyond 680, once the smaller vortex is formed, it will continue to grow. This is attributed to the effort of stronger inertia force which supports and even strengthens the small vortex not to be destroyed by the principal vortex.

During the process of breakdown of secondary vortices, the initially symmetric secondary vortex pair become asymmetric, and one of them grows much stronger to evolve the other one, such as *Figure 10f*. The inertia force supporting secondary vortices eventually diminishes, unable to maintain the symmetry. During the interaction between the two secondary vortices, one accumulates more mass and energy than the other. Once an imbalance happens between the two vortices, the destruction of the weaker one is accelerated not only by the stronger one but also by the principal vortex. Finally, the stronger secondary vortex prevails, but is soon destroyed

by the principal vortex because it is unable to resist the bigger priucipal vortex. The situation prevails when the circulation is the opposite direction from that of the principal vortex; e.g., *Figures 6c* and *9j*. In some cases, however, the secondary vortex may emerge again. This happens if the principal vortex is not strong enough to sweep through the intersection of the trailing wall with channel centreline. Therefore, the viscosity once again acts as the driving force for the inception of small vortices and the whole process repeats. The one being destroyed is that which has integrated its partner earlier. This process is observed in *Figure 9*. More investigation on the mechanism is desirable.

In summary, the balance of the Coriolis, viscous and inertia forces, and the channel geometry determine the flow patterns and the inception of flow instability.

CONCLUSIONS

A numerical study has been conducted to investigate flow instability in a laminar flow through a square channel in radial rotation. The following conclusions are derived:

(1) At an intermediate Reynolds number ($300 < Re < 680$), the longitudinal vortex pattern induced by the Coriolis force undergoes three types of flow instability. They are exhibited in the form of: (i) one vortex pair (principal vortex) at slow rotation, (ii) a formation followed by breakdown of secondary vortices near the channel centreline over the trailing wall at intermediate rotation, and (iii) restabilized principal vortex pattern in the absence of a secondary vortex at higher rotation. These instability phenomena are similar to those found in a high-aspect-ratio channel[3–7].

(2) At higher Reynolds numbers ($Re \geqslant 680$), the flow exhibits only two vortex patterns: (i) a principal vortex at slow rotation, and (ii) formation/breakdown of secondary vortices at higher rotation. However, no flow instability occurs at low Reynolds numbers ($Re \geqslant 300$).

(3) In certain cases, a repetition of the zig-zag breakdown process of secondary vortices prevails over a long flow passage. However, in most cases, the breakdown process takes place within a rather short distance.

(4) In general, the symmetry of a vortex pair prevails up to a distance 0.20 (a Re). At a low Reynolds number ($Re < 300$) and in the restabilization region, a symmetrical vortex flow prevails over the entire flow passage.

(5) Both the Coriolis force and viscous effect play a crucial role in both the mass redistribution near the channel inlet and the breakdown of the secondary vortex.

(6) Surface vorticity intensity is a measure for the incipience of a secondary vortex as well as the subsequent vortex variation.

ACKNOWLEDGEMENT

This study was supported by the Electric Power Research Institute under the EPRI Agreement RP8006-11.

REFERENCES

1 Ekman, V. W. On the influence of the Earth's rotation on ocean currents, *Arkiv. Mat. Astr. Fys.*, **2**, 1–52 (1905)
2 Tritton, D. J. *Physical Fluid Dynamics*, Van Nostrand/Reinhold, London, pp. 162–183 (1977)
3 Hart, J. E. Instability and secondary motion in a rotating channel flow, *J. Fluid Mech.*, **45**, 341–351 (1971)
4 Johnston, J. P., Halleen, R. M. and Lezius, D. K. Effects of spanwise rotation on the structure of two-dimensional fully developed turbulent channel flow, *J. Fluid Mech.*, **56**, 533–557 (1972)
5 Lezius, D. K. and Johnston, J. P. Roll-cell instabilities in rotating laminar and turbulent channel flow, *J. Fluid Mech.*, 77, 153–175 (1976)

6 Speziale, C. G. Numerical study of viscous flow in rotating rectangular ducts, *J. Fluid Mech.*, **122**, 251–271 (1982)
7 Speziale, C. G. and Thangam S., Numerical study of secondary flows and roll-cell instability in rotating channel flow, *J. Fluid Mech.*, **130**, 377–395 (1983)
8 Hwang, G. J. and Jen, T. C. Convective heat transfer in rotating isothermal ducts, *Int. J. Heat Mass Transfer*, **33**, 1817–1828 (1990)
9 Jen, T. C., Lavine, A. S. and Jwang, G. J. Simultaneously developing laminar convection in rotating isothermal square channels, *Int. J. Heat Mass Transfer*, **35**, 239–254 (1992)
10 Fann, S. and Yang, Wen-Jei, Hydrodynamically-thermally developing laminar flow through rotating channels having isothermal walls, *Num. Heat Transfer*, **22**, 257–288 (1992)
11 Fann, S., Yang, Wen-Jei and Mochizuki, S. Heat and fluid flow at entrance regions of rotating iso-heat flux channels with laminar throughflow, *Int. J. Num. Meth. Heat Fluid Flow*, **2**, 335–358 (1992)
12 Ramakrishna, K., Rubin, S. G. and Khosla, P. K. Laminar natural convection along vertical square ducts, *Num. Heat Transfer*, **5**, 59–79 (1982)
13 Chou, F. C. Combined free and forced laminar convection in horizontal rectangular channels, *PhD Thesis*, National Tsing Hua University, Taiwan (1986)
14 Patankar, S. V. *Numerical Heat Transfer and Fluid Flow*, Hemisphere, New York (1982)
15 Fann, S. Numerical and experimental studies on transport phenomena in rotating channels with throughflow, *PhD Thesis*, University of Michigan (1993)